nature communications

Article

https://doi.org/10.1038/s41467-024-52848-8

Spin-orbit entanglement driven by the Jahn-Teller effect

Received: 23 January 2024

Accepted: 19 September 2024

Published online: 08 October 2024

Check for updates

Alejandro S. Miñarro[1], Mario Villa[1], Blai Casals[1,2], Sergi Plana-Ruiz[3,4], Florencio Sánchez[1], Jaume Gázquez[1] & Gervasi Herranz[1]

Spin-orbit entanglement in 4d and 5d transition metal systems can enhance electronic correlations, leading to nontrivial ground states and the emergence of exotic excitations. There is also an interest to investigate spin-orbit entanglement in 3*d* compounds, though this is challenging due to their smaller spin-orbit coupling. Here we demonstrate that the Jahn-Teller effect in Mn^{3+} reduces the energy gap between high- and low- spin-orbital states that lead to enhanced spin-orbit entanglement. Our results show a rare example of synergistic effects of Jahn-Teller and spin-orbit interactions and provide a way to entangle different degrees of freedom in *d*-metal oxides, which may allow paths to explore the interplay of orbital, lattice and spins in 3*d* correlated systems.

Spin-orbit entanglement in transition metal oxides may result in correlated phases[1,2], like spin-orbit Mott insulators[3,4], quantum spin liquids[5–7], or excitonic magnetism[2,8–10]. All these phases rely on the emergence of strong spin-orbital textures, which require unquenched orbital momenta. In this context, the interplay between Jahn-Teller interactions and spin-orbit coupling is crucial, as the latter favors degenerate electronic eigenstates with unquenched spatial angular momenta, generally promoting spin-orbital mixing[11]. Therefore, a crucial aspect is how the orbital degeneracy is removed and how this affects spin-orbit coupling and lattice interactions[11–13]. For instance, Jahn-Teller effects in nd^5 octahedral low-spin configurations are overruled by strong spin-orbit interactions, which lift the degeneracy of the t_{2g} shells except for Kramers doublets[1,2]. The latter can interact through anisotropic bond-dependent interactions (e.g., honeycomb iridates or α−$RuCl_3$), whose ground state is a quantum spin liquid[14].

Despite their smaller spin-orbit coupling[11] spin-orbital mixing in 3*d* systems has also grabbed attention to realize spin-orbit entanglement[14–16] In this respect, intersite superexchange interactions have long been studied to entangle spin and orbital degrees of freedom in 3*d* compounds[17] notably Kugel-Khomskii models, where bond-dependent exchange interactions are inherited from the large directionality of *d* orbitals[18]. More recently, an interest has reemerged in 3*d* systems due to the possible realization of intra-site spin-orbital entanglement in d^7 systems based on Co^{2+}[15,16,19], or Ni^{3+}[20,21]. In this case, orbital degeneracy is present in t_{2g} shells, but since Jahn-Teller effects are weak in those states[22], the degeneracy is completely removed (save for Kramers degeneracy) by spin-orbit coupling, forming pseudospins from split crystal-field multiplets[23,24].

Here we discuss a different scenario, which is relevant to Mn^{3+} ions (d^4) in the $La_{2/3}Ca_{1/3}MnO_3$ perovskite. In this case, the orbital degeneracy appears in the e_g manifold, which in some systems may drive strong Jahn-Teller effects. Remarkably, we observe that spin-orbital mixing is enhanced by Jahn-Teller interactions, which is an unlikely situation in t_{2g} systems where spin-orbit and the Jahn-Teller effect are generally antagonistic (though exceptions exist for d^1 and d^3 configurations[11,25]). The underlying mechanism relies on the small energy gap (reduced by Jahn-Teller effects) between high-spin and low-spin configurations (Fig. 1). Such configurational mixing is accidental and was proposed previously to describe X-ray absorption spectra of a series of 3*d*-transition-metal oxides[26]. More recently, X-ray absorption experiments in $La_{2/3}Ca_{1/3}MnO_3$ films have been used to argue in favor of spin-orbit mixing[27]. Generally, however, mixing of t_{2g} and e_g orbitals has been considered irrelevant in most cases[28]. Here, on the contrary, we provide unambiguous evidence that Jahn-Teller instabilities promote spin-orbital entanglement in Mn^{3+} which is detected using optical wavelengths, offering further ways to explore the coupling of orbital, lattice and spins in 3*d* correlated systems.

[1]Institut de Ciència de Materials de Barcelona (ICMAB-CSIC), Campus UAB, Bellaterra, Catalonia, Spain. [2]Departament de Física Aplicada Facultat de Física, Universitat de Barcelona, Barcelona, Catalonia, Spain. [3]Scientific & Technical Resources, Universitat Rovira i Virgili, Tarragona, Catalonia, Spain. [4]LENS-MIND, Department of Electronics and Biomedical Engineering, Universitat de Barcelona, Barcelona, Catalonia, Spain. e-mail: gherranz@icmab.es

https://doi.org/10.1038/s41467-024-52848-8

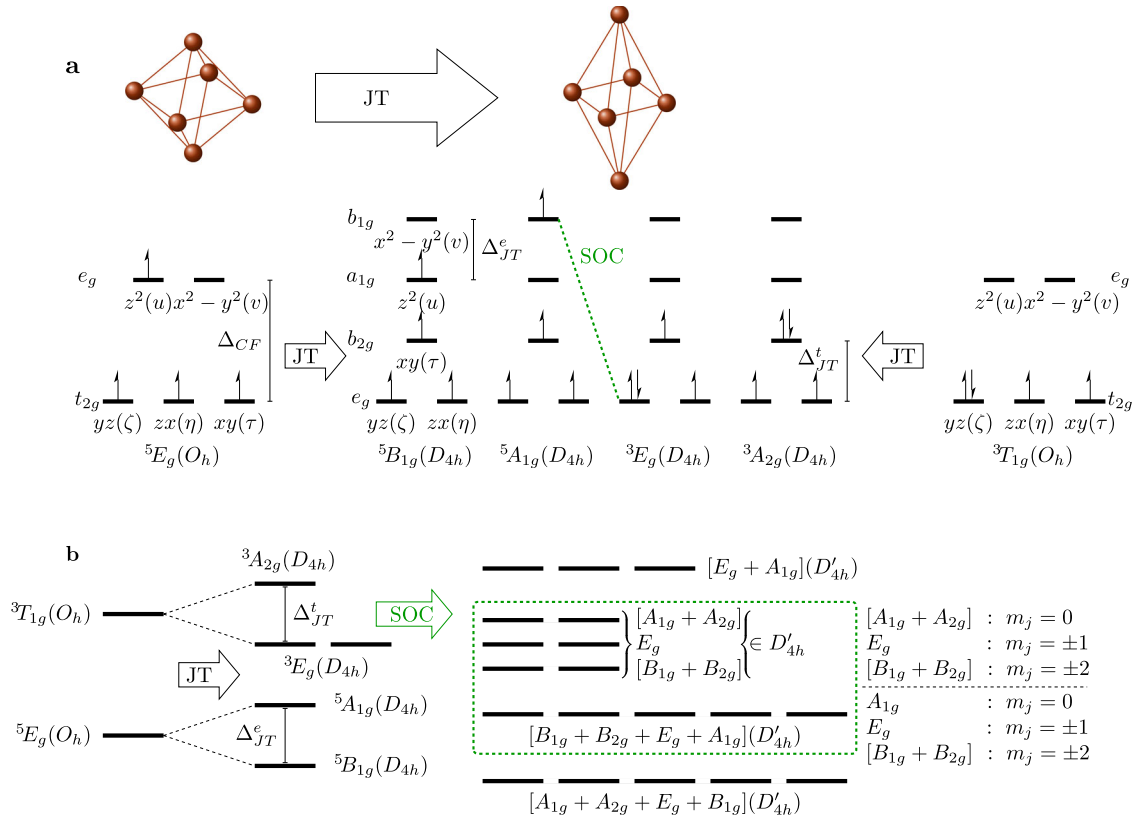

Fig. 1 | Spin-orbital entanglement in Mn^{3+} driven by the Jahn-Teller effect. **a** Occupation schemes of the 3*d*-derived orbitals of the relevant electronic states in the O_h and the Jahn-Teller elongated D_{4h} symmetry. **b** From left to right: high-spin $^5E_g(O_h)$ and low-spin $^3T_{1g}(O_h)$ states split by the Jahn-Teller effect (Δ^t_{JT}, Δ^e_{JT}), which lowers the symmetry to D_{4h}. We further indicate decomposition according to D_{4h} double group to relativistic states (denoted by D'_{4h}) and their splitting due to intra-term spin-orbit coupling (green dashed box in (**b**)). Finally, we indicate further splittings of the relativistic states due to inter-term spin-orbit coupling between the high-spin $^5A_{1g}(D_{4h})$ and the low-spin $^3E_g(D_{4h})$ terms (green-dashed SOC line in (**a**)). In the latter, the label m_j indicates the effective total angular momentum (adding spatial and spin angular momenta) along the C_4 axis of the D_{4h} structure.

Results and discussion

Origin of the $t_{2g}-e_g$ spin-orbit entanglement

To understand the underpinnings of the t_{2g}-e_g spin-orbital mixing, we consider the electronic configuration of a Mn^{3+} ion in the MnO_6 cage of the perovskite cell, which is unstable towards Jahn-Teller distortions. The states of Mn^{3+} in O_h symmetry split into high-spin $^5E_g(O_h)$ and low-spin $^3T_{1g}(O_h)$ states (Fig. 1a)[29]. The degeneracy of these sates is spontaneously broken by $E_g \times e_g$ Jahn-Teller interactions[22,30,31], which, in the case of tetragonal modes, lower the symmetry to D_{4h} (Fig. 1b). We consider tetragonal elongated distortions, which are the most stable in a large number of compounds[22] including manganites[32–35]. As a result of the Jahn-Teller effect and its lower symmetry, the energy gap between the high-spin $^5A_{1g}(D_{4h})$ and low-spin $^3E_g(D_{4h})$ states is reduced, enhancing the spin-orbit mixing through the intra-site inter-term spin-orbit coupling, see Fig. 1a. Therefore, spin-orbital mixing of t_{2g} and e_g states, which is often ignored[36], becomes prominent (though a recent work discusses t2g-eg mixing restricted to 4d/5d ions[28]) Fig. 1b also includes the double point-group representations (suitable to analyze symmetries of spin-1/2 particles under spin-orbit coupling) of both the high-spin and low-spin terms in D_{4h} point-group symmetry. From this decomposition, we see that spin-orbit coupling entangles $[B_{1g}+B_{2g}]$ double-group representations of the $^5A_{1g}(D_{4h})$ and $^3E_g(D_{4h})$ terms, as well E_g double-group pairs and A_{1g} double-group pairs of each of the two terms.

This intra-site spin-orbital entanglement is detected through optical spectroscopy as follows. Consider the $La_{2/3}Ca_{1/3}MnO_3$ compound, where correlated Jahn-Teller polarons—exhibiting short-range cooperative orbital correlations—emerge around the Curie temperature ($T_C \approx 260K$)[37]. Near the ferromagnetic transition we assume that Jahn-Teller Mn^{3+} ions are surrounded by Mn^{4+} sites. The interaction with light induces inter-site hopping between neighboring Mn^{3+}/Mn^{4+} sites through second-order virtual processes across the O atoms between the metal centers (Fig. 2a). We focus on the visible spectrum and disregard contributions from charge transfer or intra-site photoexcitations, whose resonances lie at higher frequencies[38]. The amplitudes $\alpha^{\psi_{m,i}\psi_{k,j}}_{q\hat{\epsilon}}$ for the transfer induced by light between $\psi_{m,i}$ and $\psi_{k,j}$ orbitals located at neighboring sites (i,j) are expressed as (see our ref. 29).

$$\alpha^{\psi_{m,i}\psi_{k,j}}_{q\hat{\epsilon}} = \frac{\left(t_{pd}\right)^2}{\Delta_{CT}} \sum_w P^{\psi_{k,j}}_{q\hat{\epsilon}w} \left(P^{\psi_{m,i}}_{q\hat{\epsilon}w}\right)^* \tag{1}$$

Here m,k designate the spin-orbitals that participate in the transfer and the lattice positions fulfill $\left(\vec{\mathbf{r}}_\mathbf{i} - \vec{\mathbf{r}}_\mathbf{j}\right) || \hat{\mathbf{e}}_\mathbf{q}$. In addition, $(\cdots)^*$ denotes complex conjugation, t_{pd} is the $p-d$ hopping amplitude, $\Delta_{CT} \approx 4$ eV[22] is the charge transfer energy between p and d orbitals, and the electromagnetic matrix elements $P^{\psi_{k,j}}_{q\hat{\epsilon}w}, P^{\psi_{m,i}}_{q\hat{\epsilon}w}$ involve two-center integrals:

$$P^{\psi_{k,j}(\vec{\mathbf{r}})}_{q\hat{\epsilon}w} = \left(\frac{1}{i}\int \psi_{k,j}(\vec{\mathbf{r}})\vec{\nabla}\phi_{p_w}\left(\vec{\mathbf{r}} \pm a\hat{\mathbf{e}}_\mathbf{q}\right)d\vec{\mathbf{r}}\right)\cdot\hat{\epsilon} \tag{2}$$

We use these hopping amplitudes to calculate the optical response ("Methods"). In Eqs. (1) and (2) $\hat{\mathbf{e}}_\mathbf{q}$ indicates the hopping

https://doi.org/10.1038/s41467-024-52848-8

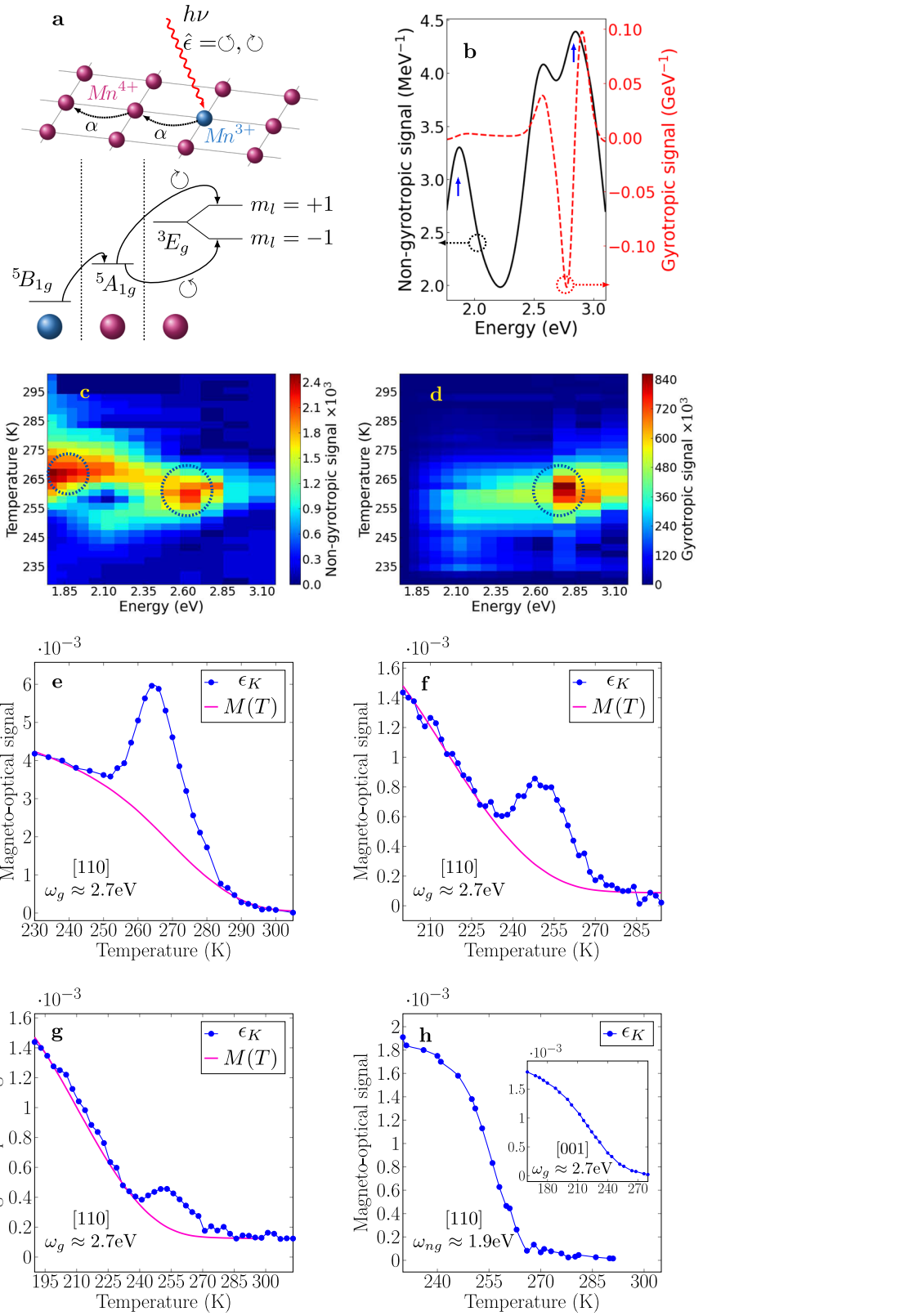

direction in the lattice, $\hat{\boldsymbol{\epsilon}}$ (generally complex) describes the polarization of light, a is the distance between Mn and O, and ϕ_{p_w} are oxygen orbitals. The key point is that the intra-site spin-orbital entanglement of e_g and t_{2g} states (namely, between high-spin $^5A_{1g}(D_{4h})$ and low-spin $^3E_g(D_{4h})$ states) drives a unique gyrotropic response, i.e., a differential response to light of opposite helicity, which induces inter-site transitions that break time reversal symmetry. Such transitions involve double group representations for initial and final states in which the total angular momentum changes by one unit, i.e., $\Delta m_j = \pm 1$ (see Fig. 1b). In consequence, spin-orbit entanglement is expected to be detected using circularly polarized light in a certain spectral region that, as it turns out, happens at optical frequencies in the case of $La_{2/3}Ca_{1/3}MnO_3$.

Fig. 2 | Optical detection of spin-orbital entanglement driven by the Jahn-Teller effect (gyrotropic response). a In the presence of light, an electron in Mn^{3+} hops to neighboring sites (Mn^{4+}) across oxygen *p*-orbitals (not shown). This transfer is described by hopping amplitudes $\alpha_{q\hat{\epsilon}}^{\psi_{m,i}\psi_{k,j}}$ between orbitals $\psi_{m,i}$ and $\psi_{k,j}$ located at adjacent site *i*, *j* (Eq. (1)). The gyrotropic response ($\circlearrowleft - \circlearrowright$) is due to the different amplitudes for left- and right- circularly polarized light ($\hat{\epsilon} \in \{\circlearrowleft, \circlearrowright\}$) that arise from inter-site transitions between high-spin ${}^5A_{1g}(D_{4h})$ and low-spin ${}^3E_g(D_{4h})$ states involving changes of angular momentum $\Delta m_l = \pm 1$. **b** Calculated nongyrotropic ($\circlearrowleft + \circlearrowright$, Eq. (5b)) and gyrotropic ($\circlearrowleft - \circlearrowright$, Eq. (5c)) spectral densities. **c**, **d** Maps of the experimental nongyrotropic ($\delta_{K,ng}$) and gyrotropic ($\delta_{K,g}$) responses, respectively, as a function of wavelength and temperature, obtained from transverse Kerr spectroscopy. The two resonances observed in (**c**) (dotted circles) are mostly contributed by nongyrotropic ${}^5B_{1g}(D_{4h}) - {}^5A_{1g}(D_{4h})$ and gyrotropic ${}^5A_{1g}(D_{4h}) - {}^3E_g(D_{4h})$ transitions, respectively (features associated with these two resonances are indicated by vertical arrows in the calculated spectra shown in (**b**)). **e** through (**h**) display the temperature dependence of the magneto-optical Kerr ellipticity ($\epsilon_K(T)$) (blue solid circles) measured in (110)-oriented films. Red solid lines ($M(T)$) in (**e**) through (**g**) are extracted (and rescaled) from fittings to SQUID measurements. The anomalous gyrotropic peaks observed in the $\epsilon_K(T)$ curves in (**e**) though (**g**) arise from the optical detection of spin-orbit entanglement driven by the Jahn-Teller effect at resonance frequencies $\omega_g \approx 2.7$ eV (${}^5A_{1g}(D_{4h}) - {}^3E_g(D_{4h})$ transition). Such anomalous peak disappears when the Kerr response is measured away from ω_g, as shown for the $\epsilon_K(T)$ curve displayed in (**h**) measured at $\omega_{ng} \approx 1.9$ eV. It is also absent in polar Kerr spectra measured at any frequency in (001) oriented films (inset of **h**). The undetected spin-orbital mixing in (001) samples is due to their particular texture of Jahn-Teller distortions and its orientation with respect to the propagation of light (see Figs. 3 and 4).

Our calculations reveal that the optical response is dominated by two contributions (shown schematically in Fig. 2a) coming, respectively, from inter-site transitions between high-spin ${}^5B_{1g}(D_{4h})$ and ${}^5A_{1g}(D_{4h})$ states and between high-spin ${}^5A_{1g}(D_{4h})$ and low-spin ${}^3E_g(D_{4h})$ states. Vertical arrows in Fig. 2b indicate the two most prominent features associated with these two transitions, which appear in the visible range. Crucially, the calculations show that a difference in the optical response to left- and right-circularly polarized light—which corresponds to the gyrotropic response represented by the red-dashed curve in Fig. 2b—only arises in the high-energy region of the visible spectrum (ca. 2.4–2.8 eV), corresponding to the inter-site transitions between high-spin ${}^5A_{1g}(D_{4h})$ and low-spin ${}^3E_g(D_{4h})$ states discussed above. We, therefore, predict the optical detection of spin-orbit entanglement in the vicinity of blue wavelengths. As described in Supplementary Note S1f, the calculation of the spectral densities shown in Fig. 2b allows to estimate the energy gap $\Delta' \sim 0.47 - 0.68$ eV between high-spin ${}^5A_{1g}(D_{4h})$ and low-spin ${}^3E_g(D_{4h})$ states, which is in reasonable agreement with the gap inferred from X-ray absorption experiments[27]. We also note that once the system interacts with light, intersite hopping induced by the electromagnetic field may reduce further the gap Δ' between high-spin and low-spin states and enhance the effects of spin-orbit mixing[29].

Optical detection of the t_{2g} – e_g spin-orbit entanglement

To verify experimentally the aforementioned predictions of optical detection of spin-orbit entanglement, we used magneto-optical Kerr spectroscopy. For reasons that will be understood below, we focus the discussion on $La_{2/3}Ca_{1/3}MnO_3$ films grown on (110)-oriented $SrTiO_3$ substrates. We first discuss transverse Kerr spectra δ_K, which, following the protocols outlined in refs. 39–41, we decomposed into gyrotropic $\delta_{K,g}$ and nongyrotropic $\delta_{K,ng}$ terms (the latter are insensitive to changes of the circularly polarized state of light). The mapping of $\delta_{K,ng}$ as a function of temperature and frequency (Fig. 2c) reveals the two predicted resonances located at $\omega_{ng} \approx 1.9$ eV and $\omega_g \approx 2.7$ eV, respectively, and are detected in a range of temperatures around $T_C \approx 260$K where correlated Jahn-Teller polarons emerge. In contrast, the gyrotropic response $\delta_{K,g}$ is only observed around $\omega_g \approx 2.7$ eV (Fig. 2d), confirming our predictions of optical detection of spin-orbit entanglement in the blue region of the visible spectrum associated with the high- to low- spin ${}^5A_{1g}(D_{4h}) - {}^3E_g(D_{4h})$ transition. Note that the ${}^5B_{1g}(D_{4h}) - {}^5A_{1g}(D_{4h})$ transition, mostly contributing to the resonance at $\omega_{ng} \approx 1.9$ eV, does not involve changes in angular momentum, hence the absence of gyrotropic signal at that frequency (although higher-order contributions may give a gyrotropic response, but they are too weak to be detected[29]). Note that the data in Fig. 2c, d, shows that the resonances appear only in a narrow range of temperatures around the Curie temperature (~250–270 K), where correlated Jahn-Teller polarons emerge. Outside this region, none of the two aforementioned resonances are detected. This observation demonstrates the existence of spin-orbit entanglement driven by the Jahn-Teller effect.

We also detected the Jahn-Teller-driven spin-orbital mixing by polar Kerr spectroscopy through the temperature dependence of the Kerr ellipticity $\epsilon_K(T)$ measured at frequency $\omega_g \approx 2.7$ eV. Polar Kerr spectroscopy is convenient because the signal is generally larger than in transverse configuration[42]. The $\epsilon_K(T)$ curves shown in Fig. 2e–g display an anomalous peak above the background around the Curie temperature ($T_C \approx 255 - 260$ K), which is the optical fingerprint of spin-orbit entanglement. These anomalous peaks disappear when the Kerr response is measured at frequencies away from the ${}^5A_{1g}(D_{4h}) - {}^3E_g(D_{4h})$ resonance ($\omega_g \approx 1.9$ eV in Fig. 2h), confirming their correlation with $t_{2g} - e_g$ entanglement. Note that the background signal, as discussed previously[39], corresponds to the conventional magneto-optical response of $La_{2/3}Ca_{1/3}MnO_3$, which is proportional to the magnetization. Importantly, we see that the breadth and height of the anomalous $\epsilon_K(T)$ curve may vary among the measured (110)-oriented films (Fig. 2e–h) but, remarkably, is absent in all polar Kerr spectra of films grown on (001)-oriented $SrTiO_3$ substrates (inset of Fig. 2h). This observation is related to the symmetry of the spin-orbit entanglement, which reveals the relevance of the geometrical configuration for its optical detection. In particular, the inter-term spin-orbit coupling between ${}^5A_{1g}(D_{4h})$ and ${}^3E_g(D_{4h})$ states connects spin-up x^2-y^2 orbitals of ${}^5A_{1g}(D_{4h})$ with spin-down *xz* orbitals of ${}^3E_g(D_{4h})$ (see green-dashed line in Fig. 1a). In consequence, the optical detection of this entanglement requires light polarized in the *x*-*y* plane. In other words, the propagation of light must have a component along the axis of the Jahn-Teller distortion, i.e., the C_4 principal axis of the distorted D_{4h} structure. This explains the variability in the amplitude of the anomalous optical response, which results from the details of the structural domain distribution and the subsequent distribution of Jahn-Teller elongations with respect to the propagation of light. This observation, as discussed in the following, is an additional evidence of the optical detection of spin-orbit entanglement.

Theoretical model

To investigate these issues, we use linear response theory. The real part of the conductivity tensor is expressed as[43],

$$\Re e\,\sigma_{\alpha\beta}(\mathbf{x},\mathbf{x}',\omega) \propto \int_{-\infty}^{+\infty} \frac{f(\varepsilon) - f(\omega+\varepsilon)}{\omega} \Big[G^R(\omega+\varepsilon) - G^A(\omega+\varepsilon)\Big] \left(\overleftrightarrow{\nabla}_{\mathbf{x}}\right)_\alpha \left(\overleftrightarrow{\nabla}_{\mathbf{x}'}\right)_\beta \Big[G^R(\omega) - G^A(\omega)\Big] d\varepsilon \tag{3}$$

where we define $\overleftrightarrow{\nabla}_{\mathbf{x}} = \frac{1}{2}\left[\frac{\partial}{\partial \boldsymbol{x}} - \frac{\overleftarrow{\partial}}{\partial \boldsymbol{x}}\right]$ with the derivative $\frac{\overleftarrow{\partial}}{\partial \boldsymbol{x}}$ acting on the left, $f(\varepsilon)$ is the Fermi-Dirac distribution, and $G^{R/A}(\omega)$ are the retarded/

https://doi.org/10.1038/s41467-024-52848-8

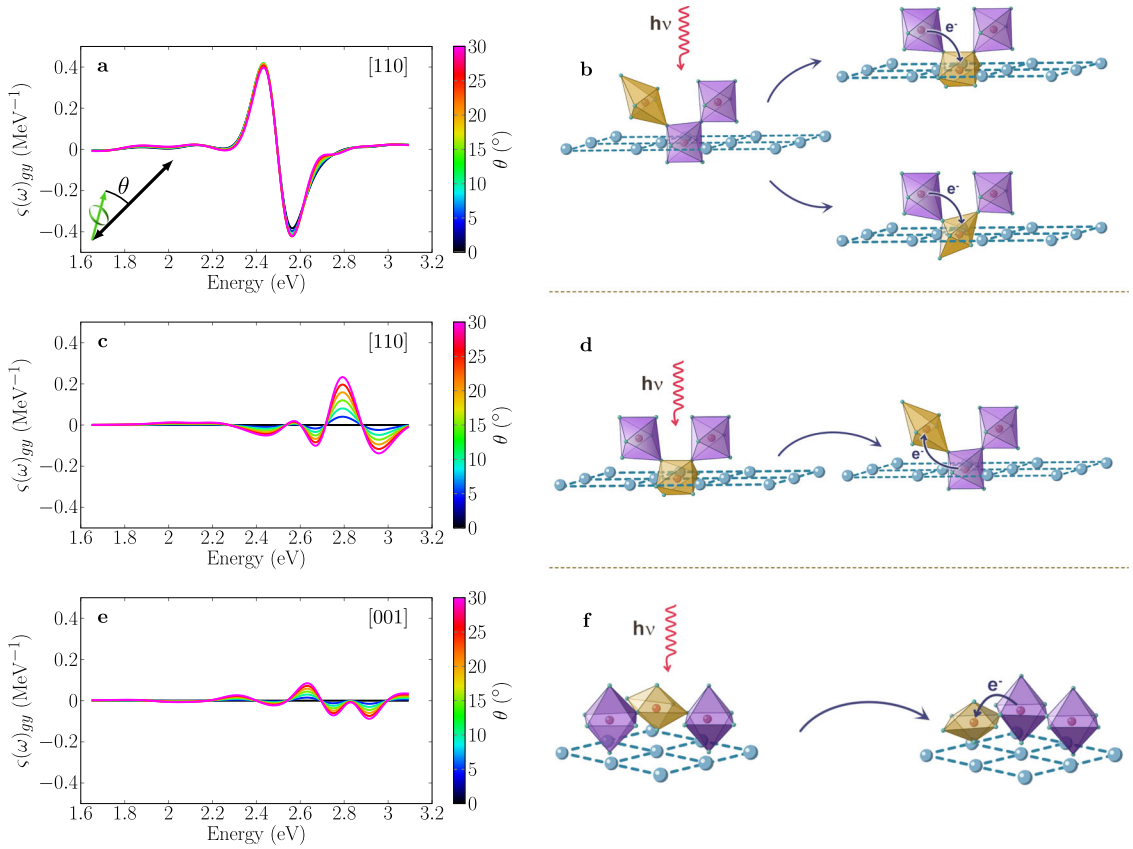

Fig. 3 | Orientational Jahn-Teller dependence of the optical detection of spin-orbit entanglement. The gyrotropic spectral function $\varsigma(\omega)_{gy} = 1/2(\varsigma(\omega)^{\circlearrowleft} - \varsigma(\omega)^{\circlearrowright})$ (defined in eq. (5)) is calculated for three relative orientations between the propagation of light and Jahn-Teller elongations (yellow-colored octahedra). Configurations (**a**, **b**) and (**c**, **d**) correspond to polar Kerr spectra in (110)-oriented films, whereas configuration (**e**, **f**) is applicable to spectra in (001) films. The calculations (left panels) are plotted for different angles $\theta \leq 30°$ (colored bars) between spins and Jahn-Teller distortions (see inset of (**a**) where θ is defined between the Jahn-Teller elongation –black double arrow– and the spin –green arrow with ring–). Cooperative effects are taken into account as follows (see sketches on the right). **b** When the initial distortion is at 45° with respect to light, the electron is transferred to a neighboring site, where the elongation may be either at 45° or at 90° with respect to light. **d** If the initial elongation is at 90°, the electron transfers to a neighboring site with the elongation at 45°. **f** Finally, when the initial elongations are at 90° with respect to light, the elongations at the transferred site are also at 90°. In this last configuration, the gyrotropic spectral function $\varsigma(\omega)_{gy}$ is much smaller (and vanishes when $\theta = 0°$, see (**e**)). This explains why spin-orbit entanglement is not detected in (001)-oriented films (inset of (**h**) in Fig. 2). The reason is that in (001) films, Jahn-Teller elongations along the propagation of light are absent, see (**f**) which follows from the structural analysis shown in Fig. 4.

advanced Green functions obtained from the diagonalization of the Hamiltonian

$$\mathcal{H} = \mathcal{H}_0 + \mathcal{H}_{JT} + \mathcal{H}_{SO} + \mathcal{H}_{e-m}^{\hat{\epsilon}=\circlearrowleft,\circlearrowright} \tag{4}$$

In Eq. (4) we include crystal field and exchange interactions in $\mathcal{H}_0$, while $\mathcal{H}_{JT}$ takes into account interactions with Jahn-Teller modes, $\mathcal{H}_{SO}$ is the spin-orbit coupling and $\mathcal{H}_{e-m}^{\hat{\epsilon}=\circlearrowleft,\circlearrowright} = \alpha_{q\hat{\epsilon}}^{\psi_{m_i}\psi_{k_j}} |\psi_{m_i}\rangle\langle\psi_{k_j}|$ describes the interaction of electrons with the electromagnetic field with hopping amplitudes $\alpha_{q\hat{\epsilon}}^{\psi_{m_i}\psi_{k_j}}$ calculated for left- ($\circlearrowleft$) and right- ($\circlearrowright$) circularly polarized light (see Eq. (1)). We use a configuration-interaction method to solve the Hamiltonian, with wavefunctions grouped by irreducible representations (Methods). The spectral functions for left/right circularly polarized light are calculated as[29]

$$\varsigma(\omega)^{\circlearrowleft,\circlearrowright} = -\frac{1}{\pi}\Im\left[G^R(\omega) - G^A(\omega)\right] = \eta/Z\pi \sum_{k,m} \frac{\left|\left\langle \psi_{5B_{1g}}|\psi_m\right\rangle\left\langle\psi_k|\psi_{5B_{1g}}\right\rangle\right|^2}{\left(\omega - \Omega_{km}\right)^2 + \eta^2} \tag{5a}$$

$$\varsigma(\omega)_{ng} = 1/2\left(\varsigma(\omega)^{\circlearrowleft} + \varsigma(\omega)^{\circlearrowright}\right) \tag{5b}$$

$$\varsigma(\omega)_{gy} = 1/2\left(\varsigma(\omega)^{\circlearrowleft} - \varsigma(\omega)^{\circlearrowright}\right) \tag{5c}$$

Here $|\psi_{5B_{1g}}\rangle$ is the initial many-electron wavefunction corresponding to the ${}^5B_{1g}(D_{4h})$ ground state, Z is the partition function, η is the reciprocal lifsssetime of the photoexcited states and $\Omega_{km} = |\omega_k - \omega_m|$ is the absolute value of the difference between eigenfrequencies. We note that before interaction with light, ${}^5A_{1g}(D_{4h})$ states are depopulated since ${}^5B_{1g}(D_{4h})$ is the ground state (see Eq. 5a). However, optical detection of spin-orbit entanglement requires that ${}^5A_{1g}(D_{4h})$ states become populated. Such mechanism is provided by the photoexcitation resonance between ${}^5B_{1g}(D_{4h})$ and ${}^5A_{1g}(D_{4h})$ states discussed above, enabling the optical detection of the spin-orbit entanglement (see also the Supplementary Information).

Equation (5c) allows us to use the spectral function $\varsigma(\omega)_{gy}$ as a means to evaluate the intensity of the gyrotropic response. For that purpose, we computed $\varsigma(\omega)_{gy}$ for different orientations of Jahn-Teller distortions with respect to the propagation of light. In the calculations (shown in Fig. 3a, c, e) we take into account Jahn-Teller cooperative effects (described schematically in Fig. 3b, d, f). Spins are quantized along the Jahn-Teller elongation, which is the C_4 principal axis of the tetragonally distorted D_{4h} structure. This is because the spatial angular momenta of the ${}^3E_g(D_{4h})$ term ($m_l = \pm 1$) are quantized along the C_4 axis, which determines the spin quantization through spin-orbit

coupling within the ${}^3E_g(D_{4h})$ term. In turn, this spin quantization is inherited by the ${}^5A_{1g}(D_{4h})$ term through its spin-orbit coupling to ${}^3E_g(D_{4h})$. This argument is consistent with neutron scattering results, which show that spins orient mostly along the Jahn-Teller elongation[44]. To allow for small deviations from full alignment observed in these experiments, we also include in Fig. 3a, c, e the dependence of $\varsigma(\omega)_{gy}$ on the angle θ between the spin orientation and Jahn-Teller distortions for angles $|\theta \leq 30°|$. In any case, the main conclusion is that $\varsigma(\omega)_{gy}$ is highly anisotropic, and confirms the expected strong dependence on the relative orientation between light propagation and Jahn-Teller elongations (Fig. 3a, c). In agreement with symmetry arguments, the anomalous gyrotropic signal becomes much smaller when Jahn-Teller elongations are oriented perpendicular to the propagation of light (and it indeed vanishes when spins fully align along the distortions, see Fig. 3e). As discussed in the following, this explains why spin-orbit mixing is not detected by polar Kerr spectroscopy in (001)-oriented films.

Structural domains and their relation to the optical detection of spin-orbit entanglement

The reason is that Jahn-Teller elongations in manganites mainly form in the plane perpendicular to the c axis of the orthorhombic cell[44] (for $La_{2/3}Ca_{1/3}MnO_3$. the space group is *Pbnm*), where $c \approx 2a_0$ and $a \approx b \approx \sqrt{2}a_0$ and a_0 is pseudocubic lattice parameter (Fig. 4a). Therefore, the c-domain structure of the films determines the relative orientation between the propagation of light and the direction of Jahn-Teller distortions in polar Kerr experiments (Fig. 4d, g). To find the domain texture we used high-angle annular dark field (HAADF) imaging in scanning transmission electron microscopy (STEM) to obtain Z contrast images. The c-axis orientation of the *Pbnm* lattice was found from the characteristic half-order reflections appearing in the fast Fourier transform, stemming from anti-polar displacements of La sites running perpendicular to the c-axis (Fig. 4b). The analysis shows that (110)-oriented films display three domains with the c-axis along the pseudocubic [001], [1$\bar{1}$0], [$\bar{1}$10] directions (Fig. 4c). Hence, for (110)-oriented samples Jahn-Teller distortions have a component along the propagation of light (Fig. 4d), which enables the optical detection of spin-orbit mixing (Fig. 4e, see also Fig. 3a, c). In contrast, (001)-oriented films exhibit a single domain epitaxy, with the c-axis oriented along [001] (Fig. 4f). In this case, Jahn-Teller distortions are in the plane of the film and subtend an angle of 90° with respect to the propagation of light (Fig. 4g). This explains why spin-orbit entanglement is not detected in (001)-oriented films (Fig. 4h and Fig. 3e). Spin-orbit mixing is there, but it cannot be detected in this optical configuration. Finally, we mapped the spatial distributions of c-axis domains in (110)-oriented films (Fig. 4i, j). Variations in the amplitude of the spin-orbit-entangled signal (Fig. 2e–h) may be attributed to different relative weights of the three domains observed in 4D-STEM diffraction maps (Fig. 4i and Supplementary Information). Therefore, the correlation between structural c-axis domains and gyrotropic response is an additional confirmation of the optical detection of spin-orbit entanglement.

In summary, we demonstrate that the Jahn-Teller effect drives spin-orbital entanglement in Mn^{3+}, which is detected using optical spectroscopies. This observation relies on the condition that the energy gap Δ' between high-spin ${}^5A_{1g}(D_{4h})$ and low-spin ${}^3E_g(D_{4h})$ states fulfills $\Delta' \approx 3/4\Delta^e_{JT}$, where Δ^e_{JT} is the Jahn-Teller gap in e_g states (see Fig. 1 and Supplementary Information for a discussion of this point). As noted in ref. 26 this condition applies to d^3 metals too (e.g., Cr_2O_3). Late-transition metals with d^n configurations ($n > 4$) have significantly larger exchange splittings and, therefore, the spin-orbital mixing is expected to be weaker. Thus, Cr or Mn-compounds (either d^3 or d^4 configurations) offer an ideal platform to investigate t_{2g} – e_g spin-orbital mixing in 3d systems. Interestingly, we have shown that $(Pr_xLa_{1-x})_{2/3}Ca_{1/3}MnO_3$ films—known to have stronger electron-lattice coupling—display optical signatures of Jahn-Teller polarons[41]. Therefore, the strength of the electron-lattice coupling can represent an additional parameter to control the intensity of spin-orbital mixing. Similar to spin-orbital exchange models[10], a theoretical analysis of quantum entanglement could be done in these materials as a function of the spin-orbital gap and coupling to the lattice. Before ending, we note that, in contrast to the conventional view considered in this work, some works assume oxygen –rather than Mn—localization for the doped holes, and propose that transitions between high-spin $(t^3_{2g}e^1_g)^5E_g\underline{t}_{2u}$ and $(t^3_{2g}e^2_g)^5T_{2g}\underline{t}_{2u}$ states may also contribute to the magneto-optic signal near the Curie temperature[45,46]. The model presented here may be further developed to consider this possibility.

Our observation opens interesting perspectives for the study of strongly correlated systems, where orbital, lattice, and spin degrees of freedom are entangled. This includes the use of electromagnetic fields to study the coherence of E ⊗ e or T ⊗ e Jahn-Teller vibronic states[12], reminiscent of the orbital waves that have been investigated in manganites or titanates (see, e.g., ref. 47). In the case analyzed here, selective photoexcitation of orbital symmetries is possible by tuning the frequency of light. In the case of Mn^{3+}, orbital selectivity is possible by tuning the wavelength of the photoexcitation, since photons with $\hbar\omega \approx 2$ eV resonate with high-spin to high-spin ${}^5B_{1g}(D_{4h}) - {}^5A_{1g}(D_{4h})$ transitions, while photons with $\hbar\omega \approx 2.7$ eV resonate with high-spin to low-spin ${}^5A_{1g}(D_{4h}) - {}^3E_g(D_{4h})$ transitions. Since the end states of each resonance have different orbital symmetries, this enables the study of orbital-selective dynamics of orbital-lattice as well of orbital-lattice-spin coupling. The last observation relies on the crucial point that orbital and lattice modes are entangled by the Jahn-Teller effect, while spins and orbitals are mixed by spin-orbit coupling. This paves the way to analyze the dynamical coupling of different degrees of freedom in a large family of materials, including manganites and their extremely rich phase diagram (charge/orbital order, complex magnetic phases, metal-insulator transitions). That may complement other spectroscopic techniques used in correlated systems which are orbital-selective, e.g., resonant inelastic X-ray scattering[47]. Note also that orbital polarization is not restricted to the Jahn-Teller effect. Indeed, other effects (e.g., crystal field) may also contribute to orbital polarization in 3d states (as in nickelates with Ni^{+1} ions[48] that could allow selective photoexcitation to study dynamical coupling of orbital, lattice and spin modes).

Methods

Theory

To study the dynamics of d-electron states subject to Jahn-Teller and spin-orbit interactions under electromagnetic fields, we solved the following Hamiltonian,

$$\mathcal{H} = \mathcal{H}_0 + \mathcal{H}_{JT} + \mathcal{H}_{SO} + \mathcal{H}^{\hat{\epsilon}=\circlearrowleft,\circlearrowright}_{e-m} \tag{6}$$

where $\mathcal{H}_0$ includes crystal field and exchange interactions, $\mathcal{H}_{JT}$ takes into account interactions with Jahn-Teller modes, $\mathcal{H}_{SO}$ is the spin-orbit coupling and $\mathcal{H}^{\hat{\epsilon}=\circlearrowleft,\circlearrowright}_{e-m}$ describes the interaction of electrons with the electromagnetic field (see Eq. (4)). In ref. 29, we fully describe this Hamiltonian and its solution using exact diagonalization. The eigenbasis for $\mathcal{H}$, used to build the retarded and advanced Green functions in Eq. (3) and (5), is constructed using a configuration interaction method, by forming linear combinations of Slater determinants of monoelectronic orbitals $t_{2g} \in (|xy\rangle, |yz\rangle, |xz\rangle)$ and $e_g \in (|x^2-y^2\rangle, |z^2\rangle)$ that comply with the Pauli exclusion principle and the point-group symmetries in orbital and spin spaces. This multi-determinant approach to build the manybody wavefunctions is appropriate for finite-size systems like the Jahn-Teller clusters considered here, and takes into account all possible virtual excitations

https://doi.org/10.1038/s41467-024-52848-8

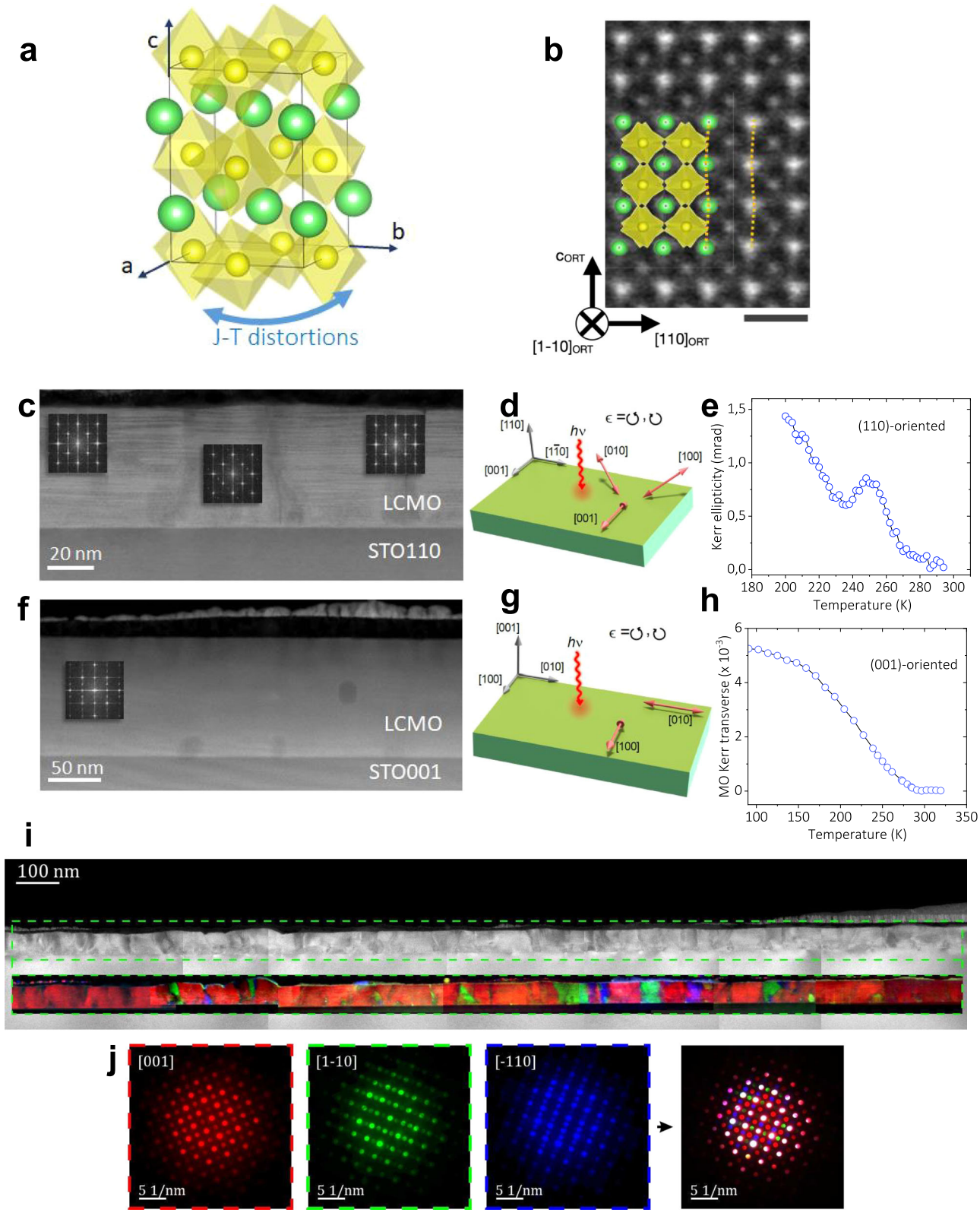

in the *d*-manifold, allowing to introduce electron correlations beyond an independent-electron approach[36,49]. This way, by building the many-electron wavefunctions as irreducible representations of pertinent point-group symmetries, we use Tanabe-Sugano diagrams where electron correlations are taken into account to compute the energies for every irreducible representation[36]. We express the eigenfunctions of the Hamiltonian $\mathcal{H}$ in terms of D_{4h} point group irreducible representations ${}^3A_{2g}(D_{4h})$, ${}^5A_{1g}(D_{4h})$, ${}^5B_{1g}(D_{4h})$ and double-group representations of the low-spin ${}^3E_g(D_{4h})$ state $[B_{1g}+B_{2g}], E_g, [A_{1g}+A_{2g}]$, where the states in $[\cdots]$ are degenerate[29]. Therefore, taking into account the spin multiplicity, the eigenbasis of the Hamiltonian $\mathcal{H}$ is 19-dimensional.

Fig. 4 | Role of the structural domains in the optical detection of spin-orbit entanglement. a Structure of the orthorhombic cell of the $La_{2/3}Ca_{1/3}MnO_3$ perovskite (P_{bnm} group space). Jahn-Teller distortions occur in the equatorial a–b plane, normal to the orthorhombic c-axis (Glazer pattern $a^-b^-c^+$). **b** Z-contrast image of a (001)-oriented film viewed along the [1$\bar{1}$0] zone axis, which allows identifying the orientation of the c-axis. The scale bar is 5 Å. **c**, **f** Show low-magnification Z-contrast images viewed along the [1$\bar{1}$0] zone axis of (110) and (001)-oriented films, respectively. Fourier transform (FT) patterns (insets) identify domains with different c-axis orientations. **d**, **g** Depiction of the propagation of light (in polar Kerr spectroscopy) with respect to the orientation of Jahn-Teller distortions inferred from c-axis maps. For (110) films, some Jahn-Teller distortions (red arrows) have a component along the propagation of light (**d**) and, therefore, exhibit an anomalous gyrotropic signal due to spin-orbit mixing (**e**). In contrast, (001) films have single domain epitaxy with the c-axis normal to the surface, which constraints Jahn-Teller distortions to the plane, perpendicular to the propagation of light (**g**). In this case, the anomalous response is absent (**h**). **i** Stitched HAADF images and processed 4D-STEM maps of a (110)-oriented film. Green-dashed rectangle indicates the region of the final orientation map (2.2 μm × 50 nm). Red corresponds to diffraction patterns in [001] zone axis, green in [1$\bar{1}$0] and blue in [$\bar{1}$10]. **j** On the left, three representative diffraction patterns used for the c-axis orientation mapping. The sum of these patterns is shown at the rightmost panel. White-colored diffraction peaks appear at the same location for all the three zone axes; those that do not coincide appear as mono-color reflections (red, green, or blue), which are used to obtain the orientation maps.

For reference, we give the explicit expression of the many-electron wavefunction for the $|\psi_{^5B_{1g}}\rangle$ ground state with spin quantum number $M=2$, using the notation defined in ref. 36.

$$|^5B_{1g}\upsilon 2\rangle = -|\zeta\eta\tau u| \tag{7}$$

The other components of M are obtained by consecutive operations of spin lowering operator and normalization, see Appendix A of ref. 29. In these expressions, we work in a product basis between orbital and spin momenta. The wavefunctions described by Eq. (7)—for general component M—are defined by kets like $|^{2S+1}G\Gamma(\gamma)M\rangle$, where S (=2 in this case) is the spin quantum number, Γ is the irreducible representation in orbital space of group $G\,(B_{1g}\,(D_{4h}))$, expressed in the basis γ (υ in Eq. (7)) and M is referred to the magnetic quantum number, $M=-S,\ldots,S$. The determinants $|\cdots|$ are expressed as $\varphi\chi$ spin-orbital functions, where the orbital angular momentum part is described by $\varphi=\zeta,\eta,\tau,u,\upsilon$ and $\chi=\alpha,\beta$ is the spinor part. The determinants are expressed using spin orbitals. The overhead bar is used to differentiate spin-down from spin-up orbitals. Accordingly, the notation inside the Slater determinants is written as $\varphi\alpha\rightarrow\varphi$ and $\varphi\beta\rightarrow\bar{\varphi}$ and $\bar{M}=-M$ for the M quantum number. The orbital part is expressed as linear combinations of spherical harmonics Y_l^m:

$$u=Y_2^0\sim\frac{1}{2}\left(3z^2-r^2\right) \tag{8a}$$

$$\upsilon=\frac{1}{\sqrt{2}}\left[Y_2^{+2}+Y_2^{-2}\right]\sim\frac{\sqrt{3}}{2}\left(x^2-y^2\right) \tag{8b}$$

$$\zeta=\frac{i}{\sqrt{2}}\left[Y_2^{+1}+Y_2^{-1}\right]\sim\sqrt{3}yz \tag{8c}$$

$$\eta=-\frac{1}{\sqrt{2}}\left[Y_2^{+1}-Y_2^{-1}\right]\sim\sqrt{3}xz \tag{8d}$$

$$\tau=-\frac{i}{\sqrt{2}}\left[Y_2^{+2}-Y_2^{-2}\right]\sim\sqrt{3}xy \tag{8e}$$

For the rest of irreducible representations, we follow the same method, which is outlined in ref. 36. In the Supplementary Information, we describe the linear combinations of Slater determinants involving low-spin ^3E_g (D_{4h}) states.

The gyrotropic spectral function defined by equation (5a) involves retarded and advanced Green functions derived from the following expressions

$$G^R=1/Z\sum_{k,m}\frac{\left|\langle\psi_{^5B_{1g}}|\psi_m\rangle\langle\psi_k|\psi_{^5B_{1g}}\rangle\right|^2}{(\omega-\Omega_{km})+i\eta} \tag{9}$$

$$G^A=1/Z\sum_{k,m}\frac{\left|\langle\psi_{^5B_{1g}}|\psi_m\rangle\langle\psi_k|\psi_{^5B_{1g}}\rangle\right|^2}{(\omega-\Omega_{km})-i\eta} \tag{10}$$

where Z is the partition function, $|\psi_{^5B_{1g}}\rangle$ is the many-electron wavefunction corresponding to the $^5B_{1g}\,(D_{4h})$ ground state in D_{4h} point symmetry (Fig. 1), and $|\psi_m\rangle$, $|\psi_k\rangle$ are wavefunctions of virtual states of the different irreducible representations that contribute to the Green functions, η being the reciprocal lifetime of these photoexcited states and $\Omega_{km}=|\omega_k-\omega_m|$ the absolute value of the difference between corresponding eigenfrequencies. The eigenfunctions $|\psi_m\rangle$, $|\psi_k\rangle$ used in equations (9) and (10) are obtained by exact diagonalization of the full Hamiltonian $\mathcal{H}$ (Eq. (6)) in a $2\times2\times2$ cluster of Mn ions with periodical boundary conditions, with a single Mn^{3+} ion in the cluster while the rest are all Mn^{4+}[29].

The matrix elements of the spin-orbit coupling term $\mathcal{H}_{SO}$ in the Hamiltonian of Eq. (6) are computed in D_{4h} point symmetry using the operator equivalent method described in ref. 36. Extensive details of this procedure are given in ref. 29.

The term $\mathcal{H}_{e-m}^{\hat{\epsilon}=\circlearrowleft,\circlearrowright}$ of the Hamiltonian gives account of the interaction of electrons with the electromagnetic field. In the model, we assume that inter-site photoexcitations consist of electrons jumping to neighboring lattice sites after interacting with light, with a photo-induced transfer described by hopping amplitudes $\alpha_{q\hat{\epsilon}}^{\psi_{m,i}\psi_{k,j}}$ defined by Eq. (1). The photoinduced transfer is dominated by hopping through p orbitals of oxygen, which requires defining many-electronic wavefunctions for the two neighboring d ions and the oxygen ligands. We use the formalism of two-center Slater-Koster integrals to derive analytic expressions for the light-induced hopping amplitudes between lattice sites (the details are given in ref. 29). In general, the resulting amplitudes will depend on the circularly polarized state of light, which is defined by the polarization vector $\hat{\epsilon}\in\{\circlearrowleft,\circlearrowright\}$. Hopping amplitudes that take complex values arise when time-reversal invariance is broken, resulting in an electromagnetic response that depends of the circularly polarized state of light, giving rise to a gyrotropic response. The model also includes Jahn-Teller cooperative effects that restrict the possible deformations of the neighboring sites where the electron is transferred[29].

The numerical calculations displayed in Figs. 2b and 3a, c, e were carried out by setting the vibronic constants to $F_E'=450$ meV, $F_T'=130$ meV and $G_E'=20$ meV (see Supplementary Note S1d). These values are in agreement with the Jahn- Teller splitting observed for e_g and t_{2g} electrons in 3d elements[22]. On the other hand, the charge transfer gap was set to $\Delta_{CT}=4$ eV[22], the reciprocal lifetime parameter $\eta=180$ meV and the $p-d$ hopping integral was set to $t_{pd}=1.2$ eV. The values of the Slater-Koster coefficients were $(sd\sigma)=1$, $(dd\sigma)=0.82$, $(dd\pi)=0.29$ and $(dd\delta)=0.07$. The spin-orbit coupling was set to $\xi_{SO}=20$ meV. The crystal field parameters were chosen to work in a region of the Tanabe-Sugano diagram appropriate for manganese ions with d^4 configuration, for which the crystal field is $10D_q\approx2$ eV and the

Racah parameter is $B \approx 0.11 - 0.13$ eV. For a detailed definition of all these parameters we refer to ref. 29.

Thin film growth

Some $La_{2/3}Ca_{1/3}MnO_3$ thin films were grown by radio frequency (RF) sputtering on (110)- and (001)-oriented $SrTiO_3$ substrates. During the deposition, substrates were held at 800 °C and pressure 330 mTorr, with an O_2/Ar pressure ratio of 1/4. After growth, samples were in-situ annealed at 800 °C for 1 h in an O_2 atmosphere at 350 Torr. The thickness ranged between $t \approx 17$ and 93 nm. Other $La_{2/3}Ca_{1/3}MnO_3$ thin films were grown by pulsed laser deposition using a KrF excimer laser. The temperature during the deposition was varied between 725 °C and 825 °C while the oxygen pressure was set to 0.3 mbar. Data in Figs. 2c, d, e and 4f, h correspond to samples grown by RF sputtering, while data in Figs. 2f, g, h and 4c, e correspond to samples grown by pulsed laser deposition. The thickness was varied by changing the number of laser pulses during the deposition, while the growth rate was determined using X-ray reflectometry. In the Supplementary Information we indicate further details on thin films growth and we discuss the optimal growth parameters to detect optically the spin-orbital entanglement driven by the Jahn-Teller effect.

Scanning electron microscopy

The local microstructure was analyzed by means of STEM on two probe-corrected microscopes, a FEI Titan 60–300 microscope and a ThermoFisher Spectra 300 both operated at 300 kV. Atomically resolved images with Z contrast were acquired by HAADF. The experiments were performed in the Laboratorio de Microscopías Avanzadas of Universidad de Zaragoza and in ALBA synchrotron. 4D-STEM diffraction maps were acquired across 100-nm and 50-nm thick layers of the prepared FIB lamellas in order to map the different crystalline orientations of the (110)-oriented $La_{2/3}Ca_{1/3}MnO_3$ thin films. These maps were acquired by scanning the electron probe and storing a diffraction pattern in each pixel. A JEOL F200 TEM ColdFEG operated at 200 kV in STEM mode was used. Probe size 6 and a 10-µm condenser aperture were selected to produce an electron probe of 1 mrad of convergence angle following the alignment method[50]. The 4D-STEM maps were acquired through the synchronization of the DigiScan 3 external scanning unit with the Gatan OneView camera via the STEMx system provided by Gatan Inc. Gatan Digital Micrograph program was used for hardware control and data processing of the 4D-STEM maps. Self-made Digital Micrograph and Matlab scripts were used to correct small pattern shifts produced when scanning the beam along large distances. The simulated diffraction patterns shown in Supplementary Information (obtained from the program ReciPro)[51] correspond to the indexation of the experimental patterns, thus the zone axes are [001] (in-plane c-axis), [1$\bar{1}$0] and [$\bar{1}$10].

X-ray reciprocal maps

X-ray reciprocal maps (discussed in Supplementary Information) were measured in a Bruker D8-Discover diffraction instrument. The maps were obtained by performing decoupled $\varpi - 2\theta$ scans at fixed φ and χ, corresponding, respectively, to the angle defining the rotation around an axis normal to the sample plane and the angle of the tilt obtained by rotating around a horizontal axis within the goniometer plane and contained within the plane of incidence. The $\varpi - 2\theta$ scans were done around particular asymmetric reflections, depending on the crystal orientation of the films. For (001)-oriented films, reciprocal space maps were collected around (103) and (130) reflections, which allowed to determine the in-plane components along pseudocubic [100] and [010] directions, while for (110)-oriented samples the maps were collected around (130) and (222) reflections, from which the two inequivalent in-plane orthogonal directions were measured, corresponding to [001] and [1$\bar{1}$0] in-plane orientations. The positions of reciprocal wavevectors Q_x (in-plane) and Q_z (out-of-plane) in the maps were determined by locating the corresponding peak maxima for both the $SrTiO_3$ substrates and the $La_{2/3}Ca_{1/3}MnO_3$ films. The shift between experimental and theoretical values were corrected. After obtaining the reciprocal vector moduli we calculated the cell parameters along the pseudocubic directions, from which the strain state of the films was measured.

Magneto-optical spectroscopy

The samples were measured in an optical transverse Kerr and polar Kerr configurations using the null-ellipsometry method to extract the magneto-optical responses[39]. In the experiments, a 150 W Xe arc lamp was used as a light source, which was dispersed by a monochromator and, after collimation, it was linearly polarized through a Glan-Thompson prism. A photoelastic modulator (PEM) was used, so that the phases of s and p-components of polarized light were modulated periodically at frequency ≈50 kHz. After PEM, the light was reflected from the samples (typical light beam diameter about ≈1 mm) and directed toward a detector through a polarizing analyzer. Finally, the signal collected from the detector is brought to a lock-in amplifier synchronized to the frequency of the PEM retardation angle φ.

The transverse Kerr signal ($\delta_K = \frac{\Delta I_p}{I_p}$), which is generally a complex magnitude, is defined by the relative change with magnetic field of the intensity I_p of p-polarized light—i.e., light with its polarization contained in the plane of incidence—upon reflection on a magnetic surface. The different parity symmetries of δ_K with respect to the applied magnetic fields—even *vs* odd—were exploited to decompose the hysteretic δ_K loops into gyrotropic magneto-optic $\delta_{K,g}$ and nongyrotropic magnetorefractive $\delta_{K,g}$ terms, respectively[39,41].

On the other hand, Kerr rotation (θ) and ellipticity (ε) were obtained as a function of temperature in the range of wavelengths $\approx 400 - 850$ nm, with s- and p-polarized light incident at angles close to the normal to the surface. In this optical arrangement, the ellipticity and rotation are given by the expressions

$$\theta_s = \frac{1}{4cJ_2(\varphi_0)}\frac{I_{2\omega,s}}{I_0}\theta_p = \frac{1}{4cJ_2(\varphi_0)}\frac{I_{2\omega,p}}{I_0} \tag{11}$$

$$\varepsilon_s = \frac{1}{4cJ_1(\varphi_0)}\frac{I_{1\omega,s}}{I_0}\varepsilon_p = \frac{1}{4cJ_1(\varphi_0)}\frac{I_{1\omega,p}}{I_0} \tag{12}$$

where $J_1(\varphi_0)$ are Bessel functions of the first kind, the PEM retardation angle is set to $\varphi_0 \approx$ ≈137.8°, I_0 is the dc-component of the detected light, and $I_{1\omega,s}, I_{1\omega,p}, I_{2\omega,s}, I_{2\omega,p}$ are the first and second harmonics of the detected light measured though the lock-in amplifier. The calibration constant c was determined experimentally.

Data availability

The data supporting this study have been deposited in Figshare (https://doi.org/10.6084/m9.figshare.24906678).

Code availability

All codes to reproduce, examine, and improve our proposed analysis are available at https://github.com/lexschz13/jtsocperovskite or from the corresponding authors upon request.

References

1. Rau, J. G., Lee, E. K.-H. & Kee, H. Y. Spin-orbit physics giving rise to novel phases in correlated systems: iridates and related materials. *Annu. Rev. Condens. Matter Phys.* **7**, 195–221 (2016).
2. Takayama, T., Chaloupka, J., Smerald, A., Khaliullin, G. & Takagi, H. Spin–orbit-entangled electronic phases in 4d and 5d transition-metal compounds. *J. Phys. Soc. Jpn.* **90**, 062001 (2021).
3. Kim, B. J. et al. Novel J_{eff} = 1/2 Mott state induced by relativistic spin-orbit coupling in Sr2IrO4. *Phys. Rev. Lett.* **101**, 076402 (2008).

4. Arita, R., Kuneš, J., Kozhevnikov, A. V., Eguiluz, A. G. & Imada, M. Ab initio studies on the interplay between spin-orbit interaction and coulomb correlation in Sr_2IrO_4 and Ba_2IrO_4. *Phys. Rev. Lett.* **108**, 086403 (2012).
5. Jackeli, G. & Khaliullin, G. Mott Insulators in the Strong Spin-Orbit Coupling Limit: From Heisenberg to a Quantum Compass and Kitaev Models. *Phys. Rev. Lett.* **102**, 017205 (2009).
6. Trebst, S. & Hickey, C. Kitaev materials. *Phys. Rep.* **950**, 1–37 (2022).
7. Kitaev, A. Anyons in an exactly solved model and beyond. *Ann. Phys.* **321**, 2–111 (2006).
8. Khaliullin, G. Excitonic magnetism in Van Vleck-type d^4 Mott insulators. *Phys. Rev. Lett.* **111**, 197201 (2013).
9. Jain, A. et al. Higgs mode and its decay in a two-dimensional antiferromagnet. *Nat. Phys.* **13**, 633–637 (2017).
10. Gotfryd, D., Pärschke, E. M., Chaloupka, J., Oleś, A. M. & Wohlfeld, K. How spin-orbital entanglement depends on the spin-orbit coupling in a Mott insulator. *Phys. Rev. Res.* **2**, 013353 (2020).
11. Streltsov, S. V. & Khomskii, D. I. Jahn-Teller effect and spin-orbit coupling: friends or foes? *Phys. Rev. X* **10**, 031043 (2020).
12. Bersuker, I. B. *The Jahn-Teller Effect* (Cambridge University Press, 2006).
13. Khomskii, D. I. & Streltsov, S. V. Orbital effects in solids: basics, recent progress, and opportunities. *Chem. Rev.* **121**, 2992–3030 (2021).
14. Winter, S. M. et al. Models and materials for generalized Kitaev magnetism. *J. Phys. Condens. Matter* **29**, 493002 (2017).
15. Liu, H. & Khaliullin, G. Pseudospin exchange interactions in d^7 cobalt compounds: possible realization of the Kitaev model. *Phys. Rev. B* **97**, 014407 (2018).
16. Sano, R., Kato, Y. & Motome, Y. Kitaev-Heisenberg Hamiltonian for high-spin d^7 Mott insulators. *Phys. Rev. B* **97**, 014408 (2018).
17. Khaliullin, G. Orbital order and fluctuations in Mott insulators. *Prog. Theor. Phys. Suppl.* **160**, 155–202 (2005).
18. Kugel, K. I. & Khomskii, D. I. The Jahn-Teller effect and magnetism: transition metal compounds. *Sov. Phys. Usp.* **25**, 231 (1982).
19. Liu, H., Chaloupka, J. & Khaliullin, G. Kitaev spin liquid in 3d transition metal compounds. *Phys. Rev. Lett.* **125**, 047201 (2020).
20. Seibel, E. M., Roudebush, J. H., Ali, M. N., Ross, K. A. & Cava, R. J. Structure and magnetic properties of the spin-1/2-based honeycomb $NaNi_2BiO_{6-\delta}$ and its hydrate $NaNi_2BiO_{6-\delta}$·1.7H_2O. *Inorg. Chem.* **53**, 10989–10995 (2014).
21. Lefrançois, E. et al. Magnetic properties of the honeycomb oxide $Na_2Co_2TeO_6$. *Phys. Rev. B* **94**, 214416 (2016).
22. Khomskii, D. I. *Transition Metal Compounds* (Cambridge University Press, 2014).
23. Kim, C., Kim, H.-S. & Park, J.-G. Spin-orbital entangled state and realization of Kitaev physics in 3d cobalt compounds: a progress report. *J. Phys. Condens. Matter* **34**, 023001 (2022).
24. Liu, X. & Kee, H. Y. Non-Kitaev versus Kitaev honeycomb cobaltates. *Phys. Rev. B* **107**, 054420 (2023).
25. Streltsov, S. V., Temnikov, F. V., Kugel, K. I. & Khomskii, D. I. Interplay of the Jahn-Teller effect and spin-orbit coupling: the case of trigonal vibrations. *Phys. Rev. B* **105**, 205142 (2022).
26. de Groot, F. M. F. et al. Oxygen 1s x-ray-absorption edges of transition-metal oxides. *Phys. Rev. B* **40**, 5715 (1989).
27. Huang, S. W. et al. Polaronic effect in the x-ray absorption spectra of $La_{1-x}Ca_xMnO_3$ manganites. *J. Phys. Condens. Matter* **31**, 195601 (2019).
28. Stamokostas, G. L. & Fiete, G. A. Mixing of t_{2g}–e_g orbitals in 4d and 5d transition metal oxides. *Phys. Rev. B* **97**, 085150 (2018).
29. Miñarro, A. S. & Herranz, G. Jahn-Teller states mixed by spin-orbit coupling in an electromagnetic field. *Phys. Rev. B* **106**, 165108 (2022).
30. Griffith, J. S. *The Theory of Transition-Metal Ions* (Cambridge University Press, 2009).
31. Ederer, C., Lin, C. & Millis, A. J. Structural distortions and model Hamiltonian parameters: from LSDA to a tight-binding description of $LaMnO_3$. *Phys. Rev. B* **76**, 155105 (2007).
32. Louca, D., Egami, T., Brosha, E. L., Röder, H. & Bishop, A. R. Local Jahn-Teller distortion in $La_{1-x}Sr_xMnO_3$ observed by pulsed neutron diffraction. *Phys. Rev. B* **56**, R8475 (1997).
33. Proffen, T., DiFrancesco, R. G., Billinge, S. J. L., Brosha, E. L. & Kwei, G. H. Measurement of the local Jahn-Teller distortion in $LaMnO_{3.006}$. *Phys. Rev. B* **60**, 9973 (1999).
34. Sartbaeva, A., Wells, S. A., Thorpe, M. F., Božin, E. S. & Billinge, S. J. L. Geometric simulation of perovskite frameworks with Jahn-Teller distortions: applications to the cubic manganites. *Phys. Rev. Lett.* **97**, 065501 (2006).
35. Chen, W.-T. et al. Striping of orbital-order with charge-disorder in optimally doped manganites. *Nat. Commun.* **12**, 6319 (2021).
36. Sugano, S., Tanabe, Y. & Kamimura, H. *Multiplets of Transition-Metal Ions in Crystals* (Academic Press New York, 1970, 2009).
37. Adams, C. P., Lynn, J. W., Mukovskii, Y. M., Arsenov, A. A. & Shulyatev, D. A. Charge ordering and polaron formation in the magnetoresistive oxide $La_{0.7}Ca_{0.3}MnO_3$. *Phys. Rev. Lett.* **85**, 3954 (2000).
38. Rusydi, A. et al. Metal-insulator transition in manganites: changes in optical conductivity up to 22 eV. *Phys. Rev. B* **78**, 125110 (2008).
39. Casals, B. et al. Giant optical polarization rotation induced by spin-orbit coupling in polarons. *Phys. Rev. Lett.* **117**, 026401 (2016).
40. Caicedo, J. M., Dekker, M. C., Dörr, K., Fontcuberta, J. & Herranz, G. Strong magnetorefractive and quadratic magneto-optical effects in $(Pr_{0.4}La_{0.6})_{0.7}Ca_{0.3}MnO_3$. *Phys. Rev. B* **82**, 140410(R) (2010).
41. Caicedo, J. M., Fontcuberta, J. & Herranz, G. Magnetopolaron-induced optical response in transition metal oxides. *Phys. Rev. B* **89**, 045121 (2014).
42. Zvezdin, A. & Kotov, V. *Modern Magnetooptics and Magnetooptical Materials*. (Taylor & Francis, London, 1997).
43. Rammer, J. *Quantum Field Theory of Non-Equilibrium States* (Cambridge University Press 2007). Note that the imaginary part of the conductivity tensor is related to the real part by the Kramers-Kronig relation $\Re e\,\sigma_{\alpha\beta}(\boldsymbol{x},\boldsymbol{x}',\omega) = \frac{1}{\pi} P\int_{-\infty}^{+\infty} d\omega' \frac{\Im m\,\sigma_{\alpha\beta}(\boldsymbol{x},\boldsymbol{x}',\omega')}{\omega'-\omega}$, where P denotes the principal value.
44. Xiong, X. et al. Correlation between coherent Jahn-Teller distortion and magnetic spin orientation in $La_{1-x}Sr_xMnO_3$. *Phys. Rev. B* **60**, 10186 (1999).
45. Gan'shina, E. A., Vashuk, M. V., Vinogradov, A. N. & Mukovskii, Ya. M. Experimental evidence of the electronic transitions responsible for magneto-optical activity of $La_{1-x}Sr_xMnO_3$ ($x \le 0.25$). *J. Magn. Magn. Mater.* **300**, e126–e12 (2006).
46. Gan'shina, E. et al. Optical and magneto-optical spectroscopy of manganites. *J. Magn. Magn. Mater.* **300**, 62–66 (2006).
47. Ament, L. J. P., van Veenendaal, M., Devereaux, T. P., Hill, J. P. & van den Brink, J. Resonant inelastic x-ray scattering studies of elementary excitations. *Rev. Mod. Phys.* **83**, 705–767 (2011).
48. Li, D. et al. Superconductivity in an infinite-layer nickelate. *Nature* **572**, 624–627 (2019).
49. Szabo, A. & Ostlund, N. S. Modern. *Quantum Chemistry: Introduction to Advanced Electronic Structure Theory* (Dover Publications Inc., 1996).
50. Plana-Ruiz, S. et al. Quasi-parallel precession diffraction: alignment method for scanning transmission electron microscopes. *Ultramicroscopy* **193**, 39–51 (2018).
51. Seto, Y. & Ohtsuka, M. ReciPro: free and open-source multipurpose crystallographic software integrating a crystal model database and viewer, diffraction and microscopy simulators, and diffraction data analysis tools. *J. Appl. Cryst.* **55**, 397–410 (2022).

Acknowledgements
We acknowledge financial support from Projects No. PID2023-152225NB-I00, PID2023-147211OB-C21, PID2020-118479RBI00, PID2020-112548RB-I00, and Severo Ochoa MATRANS42 (No. CEX2023-001263-S) of the Spanish Ministry of Science and Innovation (Grant No. MICIU/AEI/10.13039/501100011033 and FEDER, EU)"), Projects No. TED2021-129857B-I00 and TED2021-130453B-C21, funded by MCIN/AEI/10.13039/501100011033 and European Union NextGeneration EU/PRTR and by the Generalitat de Catalunya (2021 SGR 00445, 2021 SGR 00804). We thank the X-ray Diffraction Laboratory at ICMAB-CSIC for their assistance in X-ray diffraction reciprocal space maps. We thank Gyanendra Singh for his participation in formatting some of the figures of the main text. EM02-METCAM at ALBA and ICTS-CNME at UCM are acknowledged for offering access to STEM microscopy and expertise. The authors acknowledge the TEM facilities of the Scientific & Technical Resources Service (SRCiT) from Universitat Rovira i Virgili where the TEM was partially funded by the operative program FEDER Catalunya 2014-2020 (IU16-015844).

Author contributions
B.C. performed magneto-optical spectroscopy and analyzed their data. G.H. and A.S.M. developed the theory. A.S.M. developed mathematical formulations, wrote the codes, and ran the simulations and the post-processing codes to analyze the data from calculations. A.S.M. analyzed and processed the data from X-ray reciprocal maps. F.S. supervised the growth of the thin films by pulsed laser deposition. J.G. and M.V. performed STEM measurements, including HAADF and data analysis. S.P.R. and J.G. participated in 4D-STEM map experiments, and S.P.R. analyzed and processed the data from 4D-STEM. G.H. supervised the project and wrote the paper.

Competing interests
The authors declare no competing interests.

Additional information
Supplementary information The online version contains supplementary material available at https://doi.org/10.1038/s41467-024-52848-8.

Correspondence and requests for materials should be addressed to Gervasi Herranz.

Peer review information *Nature Communications* thanks Woojin Kim, and the other, anonymous, reviewers for their contribution to the peer review of this work. A peer review file is available.